

## Research



**Cite this article:** Stocking JB, Laforsch C, Sigl R, Reidenbach MA. 2018 The role of turbulent hydrodynamics and surface morphology on heat and mass transfer in corals. *J. R. Soc. Interface* **15**: 20180448.  
<http://dx.doi.org/10.1098/rsif.2018.0448>

Received: 15 June 2018  
Accepted: 20 November 2018

**Subject Category:**  
Life Sciences—Physics interface

**Subject Areas:**  
biophysics, environmental science

**Keywords:**  
corals, heat and mass transfer, turbulence, oscillatory flow, roughness, biological fluid mechanics

**Author for correspondence:**  
Jonathan B. Stocking  
e-mail: [jbs4yq@virginia.edu](mailto:jbs4yq@virginia.edu)

Electronic supplementary material is available online at <https://dx.doi.org/10.6084/m9.figshare.c.4320977>.

# The role of turbulent hydrodynamics and surface morphology on heat and mass transfer in corals

Jonathan B. Stocking<sup>1</sup>, Christian Laforsch<sup>3</sup>, Robert Sigl<sup>3</sup>  
and Matthew A. Reidenbach<sup>2</sup>

<sup>1</sup>Department of Mechanical and Aerospace Engineering, and <sup>2</sup>Department of Environmental Sciences, University of Virginia, Charlottesville, VA 22903, USA

<sup>3</sup>Animal Ecology I and BayCEER, University of Bayreuth, Bayreuth 95440, Germany

JBS, 0000-0003-1309-0263

Corals require efficient heat and mass transfer with the overlying water column to support key biological processes, such as nutrient uptake and mitigation of thermal stress. Transfer rates are primarily determined by flow conditions, coral morphology and the physics of the resulting fluid–structure interaction, yet the relationship among these parameters is poorly understood especially for wave-dominated coral habitats. To investigate the interactive effects of these factors on fluxes of heat and mass, we measure hydrodynamic characteristics *in situ* over three distinct surface morphologies of massive stony corals in a Panamanian reef. Additionally, we implement a numerical model of flow and thermal transport for both current and wave conditions past a natural coral surface, as well as past three simplified coral morphologies with varying ratios of surface roughness spacing-to-height. We find oscillatory flow enhances rates of heat and mass transfer by 1.2–2.0× compared with unidirectional flow. Additionally, increases in Reynolds number and in surface roughness ratio produce up to a 3.3× and a 2.0× enhancement, respectively. However, as waves begin to dominate the flow regime relative to unidirectional currents, the underlying physical mechanisms mediating transfer rates shift from predominantly turbulence-driven to greater control by inertial accelerations, resulting in larger heat and mass transfer for small surface roughness ratios. We show that for rough corals in wave-dominated flows, novel trade-off dynamics for heat and mass transfer exist between broadly spaced roughness that enhances turbulence production versus narrowly spaced roughness that produces greater surface area. These findings have important implications for differential survivorship during heat-induced coral bleaching, particularly as thermal stress events become increasingly common with global climate change.

## 1. Introduction

Coral growth and sustainability depend on the efficient exchange of heat and mass between the water column and the coral surface [1]. As sessile organisms within benthic reef communities, corals rely on wave- and current-induced fluid advection to supply the input of nutrients and dissolved gasses (e.g.  $\text{NH}_4^+$ ,  $\text{PO}_4^{3-}$ ,  $\text{CO}_2$  and  $\text{O}_2$ ) required for calcification [2], metabolism [3] and endosymbiont photosynthesis [4]. Additionally, fluid motion drives efflux processes such as waste removal [5], larval transport [6] and mitigation of absorbed solar irradiance to alleviate thermal-induced bleaching [7]. Rates of heat ( $q$ ) and mass ( $q_m$ ) transfer are controlled at the coral–water interface by the thermal boundary layer (TBL) and the concentration boundary layer (CBL), respectively. The thickness of the TBL and CBL, in conjunction with the diffusivities of heat and mass, determine the efficiency of scalar transport. As the TBL and CBL are typically only microns thin, experimental measurements of temporal and spatial dynamics are challenging. However, empirical work has shown that

heat and mass flux are enhanced by a thinning of boundary layers, which can be caused by increased surface shear stress from high-speed flow [8] and/or disruptions by turbulent sweeps and ejections [9]. Surface morphology has also been shown to produce spatial variability in the size of the CBL [10], indicating that both flow conditions and surface roughness are important controls on heat and mass transfer. The impacts of these small-scale diffusion boundary layers have been shown to link directly to large-scale coral ecology where, for example, spatial variation in boundary layer size resulting from flow speed [11] and reef structure [12] drives differential survivorship during thermal stress-induced bleaching events. Critically, these types of bleaching events are predicted to occur with increasing frequency and intensity as sea surface temperatures rise due to climate change [13].

At length scales beyond CBL or TBL dynamics—for example, at the organismal- or reef-scale—flow velocities have been shown, in the absence of wave action, to correlate with rates of mass transfer according to  $\sim U_b^{3/4}$ , where  $U_b$  is the bulk current speed [14]. Given the range of flow speeds commonly found in reefs, this scaling suggests an approximately 4–5× enhancement in mass flux from higher velocities alone [15]. For the oligotrophic tropical habitats in which corals are typically found, uptake of dissolved nutrients across a reef flat often occurs at the physical limits of mass transfer [16]. This ‘mass-transfer limitation’ implies that reaction kinetics of metabolic processes do not pose a biological resistance to mass transfer and that enhanced flux directly promotes production and growth. Flow conditions, thus, can drive short-term morphological plasticity resulting in branch thickening, increased compactness, and enhanced skeletal density for corals living in high-speed flow environments [1]. However, excessively fast flows can impair particulate food capture [17] and physically damage reef structures [18].

Coral habitats typically feature significant wave activity, whose unsteady pressure fields induce oscillatory flows at the benthos, and which acts to enhance rates of mass transfer 2–3× for coral canopies compared with equivalent unidirectional flow speeds [19,20]. The dominant wave period  $T$  also affects the degree of oscillatory flow enhancement, such that a large  $T$  approximates the underlying physics and mass transfer rates of unidirectional flow, whereas shorter wave periods enhance the influence of inertial effects causing local accelerations that reduce the CBL and enhance mass transfer [21]. However, when comparing wave and current conditions that produce equivalent bed shear stresses—which have been shown to correlate with mass transfer rates according to  $q_m \propto \tau_b^{0.4}$ —oscillatory flow enhances mass transfer rates by only approximately 10% [22]. The underlying physics of the wave–structure interaction responsible for this enhancement and its variance, especially with regard to different surface types, is not well explained by the existing literature.

At the length scale of an individual coral, drag-dominated unidirectional flow and inertia-dominated oscillatory flow produce different magnitudes and spatial-temporal patterns of surface shear stresses, which control the TBL/CBL thickness and associated heat/mass flux. The relative influence of drag and inertia forces on a bluff body—such as an isolated coral head—exposed to oscillatory flow is described by two non-dimensional parameters: the Keulegan–Carpenter ( $KC$ ) number and the frequency parameter ( $\beta$ ), also called the

Stokes number. In physical terms, the  $KC$  number describes the fluid particle excursion length, before flow reversal, relative to the object length and is given by  $KC = U_{\max}T/L$ , where  $U_{\max}$  is the amplitude of the oscillatory flow and  $L$  is the characteristic body length scale.  $\beta$  describes the influence of fluid oscillation relative to momentum damping by fluid viscosity and is given by  $\beta = fL^2/\nu$ , where  $f$  is the frequency of oscillation and  $\nu$  is fluid viscosity [23]. The specific combination of  $KC$  and  $\beta$  determines the pattern of vortex shedding from an object in unsteady flow and the associated wall shear forces [24]. For a fixed frequency parameter, small values of  $KC$  (e.g.  $KC < 7$ ) produce greater inertial forces relative to drag forces, whereas for large  $KC$  (e.g.  $KC > 9$ ), the influence of forces is reversed, with drag dominating inertial effects [25]. Since wall shear forces have been shown to correlate with mass transfer rates, the values of  $KC$  and  $\beta$  play an integral role in determining the physics of the fluid–structure interaction and help drive the dynamics of heat and mass exchange.

In addition to flow speed and oscillation, the surface roughness of a coral plays a critical role in determining the near-surface flow structure, as well as the amount of surface area available for scalar flux. Surface morphologies of massive, i.e. hemispheric, coral species exhibit broad phenotypic diversity (figure 1*a–c*) and can be described by the height  $k$  and spacing  $w$  between individual roughness elements on the surface. A useful way to characterize surface roughness is by analogy to engineered surfaces such as two-dimensional bar roughness, which categorizes roughness based on the spacing-to-height ratio between roughness elements, i.e.  $w/k$ . Densely packed roughness with  $w/k < 1$  is historically called ‘*d*-type’ (figure 1*d*) and exhibits stable intra-cavity vortices, which lack momentum transfer to the overlying boundary layer [26]. By contrast, broadly spaced roughness with  $w/k > 1$  is called ‘*k*-type’ (figure 1*e*) and features vortex ejection into the boundary layer flow. Recent direct numerical simulations suggest a more appropriate classification is based on the relative contribution of frictional and pressure drag, with friction dominating for *d*-type and pressure, or form drag, dominating for *k*-type [27]. Regardless of classification metric, maximizing heat or mass transfer across a topographically rough surface inherently involves trade-offs between increasing the total available surface area for flux (as exemplified by very dense, low  $w/k$  ratio roughness) versus enhancing convective transport due to turbulence production (as best achieved through broadly spaced, high  $w/k$  ratio roughness).

The unique flow environment of corals—i.e. wave-driven, shallow, near-shore—and the phenotypic variation of surface morphologies among corals create interactive effects between flow and topography that remain poorly understood with regard to both the underlying physics of the fluid–structure interaction and the associated impact on heat and mass flux. This paper seeks to address key unanswered questions of how coral surface roughness affects heat transfer under conditions of both steady and oscillatory flow. Specific questions include:

- (1) How do particular  $w/k$  roughness ratios on the surface of a hemispheric coral alter heat and mass transfer rates across a range of flow conditions with distinct  $KC$  and  $\beta$  parameters?
- (2) What underlying physical mechanisms govern the trade-offs between turbulence production and available

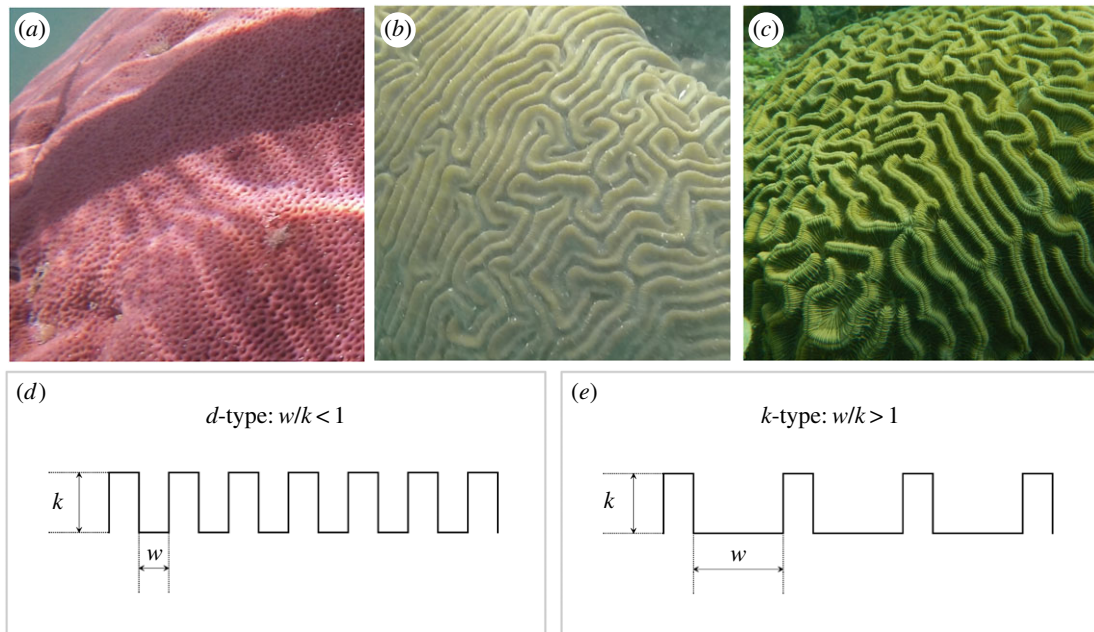


**Figure 1.** Photographs of massive scleractinian corals studied, highlighting phenotypic diversity of surface morphology, and schematics of two-dimensional bar roughness as idealized engineering analogue. (a) *Siderastrea siderea* with smooth surface, (b) *Diploria labyrinthiformis* with densely packed roughness, and (c) *Colpophyllia natans* with broadly spaced roughness. (d) *d*-type roughness with narrow spacing  $w$ , producing a large surface area. (e) *k*-type roughness with wide spacing  $w$ , producing a small surface area.

surface area that are responsible for optimizing heat and mass flux?

These questions were addressed through a combination of field measurements within a coral reef in Panama and a hydrodynamic-thermal energy numerical model implementing large eddy simulations (LES) of flow past corals with idealized surface roughness (and validated using velocimetry measurements in a laboratory water tunnel). By applying the heat–mass analogy for convection coefficients, we convert results of interfacial heat flux to estimates of equivalent rates of mass flux, under the assumption of a mass-transfer limited system. Our findings indicate that the particular surface roughness type that maximizes total heat transfer across the coral surface varies according to flow condition. Further, the relative influence of drag and inertial forces—as determined by the  $KC$  and  $\beta$  numbers of the flow–structure interaction—plays a critical role in the physical mechanisms that govern the efficiency of heat and mass transfer. Such findings have important ramifications for coral growth and resilience, habitat distribution, and long-term selective evolutionary pressures.

## 2. Material and methods

### 2.1. Field site and species morphology

Velocity measurements over three species of massive scleractinian corals were obtained in a fringing coral reef in Bocas del Toro, Panama during two field deployments in June 2012 and July 2013. The study site ( $9^{\circ}21' N$ ,  $82^{\circ}16' W$ ) is located in Almirante Bay approximately 50 m off the shore of Isla Colón near the Smithsonian Tropical Research Institute. The reef at the field location is exposed to mixed semidiurnal tides with a range of approximately 0.5 m [28], and wave conditions are primarily wind-driven from the southeast. A wave and tide logger (TWR-2050; RBR Ltd, Canada) recorded wave heights and water depth at 10 min intervals with a burst length of 1024 samples and rate

of 4 Hz. Mean wave heights ranged between 2–20 cm, and water column depth measured approximately 1.0–2.5 m.

The three species of corals studied were selected based on differences in their surface morphology: *Siderastrea siderea* (figure 1a), which has a smooth, slightly dimpled surface; *Diploria labyrinthiformis* (figure 1b), commonly known as grooved brain coral and possessing densely spaced ridges similar to *d*-type roughness; and *Colpophyllia natans* (figure 1c), commonly known as boulder brain coral and possessing broadly spaced ridges similar to *k*-type roughness. Surface ridges on the two brain coral species are highly irregular, but estimates of average roughness spacing-to-height ratio  $w/k$  were made using 10 measurement locations on each coral. *Diploria labyrinthiformis* had an average roughness spacing of  $3 \pm 0.7$  mm (mean  $\pm$  standard deviation) and a roughness height of  $3.7 \pm 0.9$  mm, which yields a  $w/k$  ratio of approximately 0.8, within the range traditionally defined as *d*-type. *Colpophyllia natans* had an average roughness spacing of  $7 \pm 3.9$  mm and a roughness height of  $6 \pm 1.3$  mm, which yields a  $w/k$  ratio of approximately 1.2, within the range traditionally defined as *k*-type.

### 2.2. Instrumentation

A profiling acoustic Doppler velocimeter (ADV) (Vectrino Profiler; Nortek AS, Norway) was used to obtain three-component velocity measurements (horizontal  $u$ , lateral  $v$  and vertical  $w$ ) over each of the coral species. The ADV recorded approximately 3 cm vertical profiles of the turbulent boundary layer adjacent to the coral surface at a resolution of 1 mm. Velocity records were sampled at 25 Hz for a measurement period ranging between 5–10 min (7 500–15 000 samples per record), a time length previously shown to best balance the need to obtain convergence of turbulence statistics while maintaining stationarity of wave and tide conditions [29]. Stationarity of tidal flow for each record was confirmed using the non-parametric reverse arrangements test ( $N = 10$ ,  $\alpha = 0.05$ ; [30]), and each record was rotated into the dominant streamwise direction  $u$  for post-processing.

The ADV was attached to an aluminium frame with length and width of 1 m and height-adjustable legs to accommodate instrument tilt. Though non-local turbulence has been shown

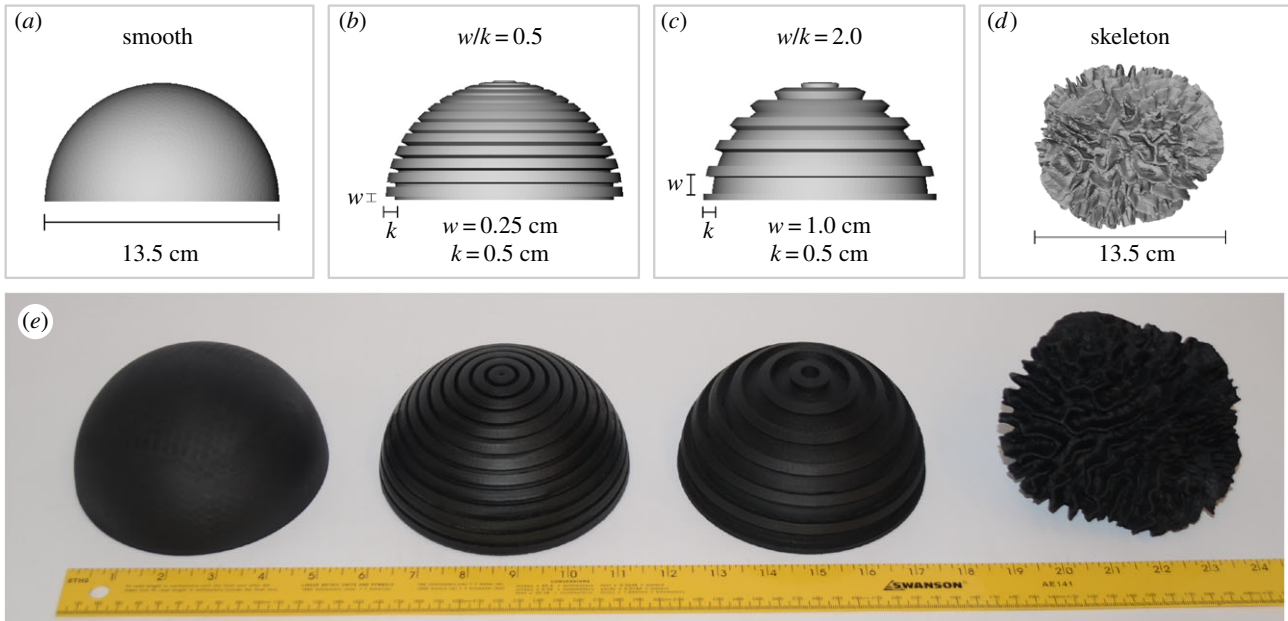


**Figure 2.** Digital and 3D-printed coral models with idealized surface bar roughness and a natural skeleton morphology. (a) Smooth surface, (b) *d*-type morphology, (c) *k*-type morphology, (d) CT-scanned *Platygyra* skeleton, (e) 3D-printed physical models for water tunnel testing. (Online version in colour.)

to have minimal effect on mass transfer coefficients [31], in order to minimize this influence from other reef features and the test frame legs, spatially isolated corals were selected for testing, and the frame was positioned in-line with the dominant flow direction. ADV measurements near boundaries can be biased due to interference from reflected acoustic pulses [32], and this bias can be identified by a sharp increase in the signal-to-noise ratio (SNR). The vertical range of echo contamination was determined by locating the measurement bin at which the mean SNR transitions from decreasing to increasing, and this region of less reliable data (typically only approximately 3 mm) is indicated by hatched grey regions in the plots of ADV results.

### 2.3. Data analysis and turbulence statistics

To isolate the mass- and momentum-transferring turbulent motions from the irrotational wave orbital motions, each velocity record was decomposed into its component parts via a spectral separation technique called the Phase Method [33]. The Phase Method converts the temporal record into frequency space using Fourier transforms and isolates the wave stress, evident as a spike in the power spectrum above the  $-5/3$  inertial layer resulting from turbulence. (Stocking *et al.* [34] contain additional details about the method implementation.) Once isolated, turbulence stress components were used to estimate Reynolds shear stress  $\overline{u'w'}$  and total turbulent kinetic energy  $\text{TKE} = 0.5(\overline{u'u'} + \overline{v'v'} + \overline{w'w'})$ , where the prime notation indicates instantaneous turbulence fluctuations and the overbar represents time-averaging.

Total bed shear stress  $\tau_b$  resulting from the combined wave-current boundary layer was calculated using independent contributions of current-only bed shear  $\tau_c$  and wave-driven near-bed oscillatory flow bed shear  $\tau_w$ , according to  $\tau_b = \sqrt{\tau_c^2 + \tau_w^2}$  [35]. Current-only bed shear was parametrized using near-bed TKE according to  $\tau_c = 0.19\rho\text{TKE}$  [36], while wave-only bed shear was parametrized using orbital wave velocity  $\tilde{u}_{om}$  and a local friction factor  $f_w$  according to  $\tau_w = 0.5\rho f_w \tilde{u}_{om}$  [37]. Combined wave-current bed shear was then used to estimate and compare rates of mass and heat flux across coral surface morphologies, according to  $q_m \propto \tau_b^{0.4}$  based on previously established correlations [38].

### 2.4. Digital models of natural and idealized corals

For the hydrodynamic-thermal numerical simulations, three computer models representing idealized corals—a smooth coral, a coral with *d*-type roughness ( $w/k = 0.5$ ), and a coral with *k*-type roughness ( $w/k = 2.0$ ) (figure 2*a–c*)—were designed using a parametric three-dimensional computer-aided design modeller (FreeCAD v. 0.15, 2015). All models had a diameter of 13.5 cm and a height of 6.75 cm, inclusive of roughness. The rough models each had surface ridges extending 0.5 cm in height with a spacing of 0.25 cm and 1.0 cm for the *d*-type and *k*-type, respectively. Roughness features were implemented as concentric rings to eliminate radial flow dependence and to simplify the highly tortuous surface roughness of natural corals.

As a natural morphology for comparison, a fourth computer model was created using a high-resolution X-ray computed tomography (CT) scan of a skeleton of a *Platygyra* coral on loan from the Zoologische Staatssammlung München (figure 2*d*). Due to export controls, none of the corals from the Panamanian reef were available for CT scanning. The *Platygyra* skeleton was selected as its morphology is most similar to the *C. natans* corals studied in Panama. The scan was performed on a Siemens Somatom Emotion 16 CT scanner (Siemens Healthcare GmbH; Erlangen, Germany) at a tube voltage of 110 kV (Eff mAs 64) and spatial resolution of  $0.46 \times 0.46$  mm with a slice thickness of 0.75 mm. Hounsfield units (HU; standard computed tomography units), which correspond to average X-ray attenuation values, ranged from  $-1024$  to  $+3071$  and were set at 0 for water and  $-1000$  for air. Post-processing and 3D reconstruction was performed using the AMIRA 5.5 software package (FEI Visualization Sciences Group, SAS; Mérégnac Cedex, France). No filters were used prior to image processing of the volume data. Surface area rendering was carried out by iso-contouring, which generates iso-surfaces within a three-dimensional scalar field with regular Cartesian coordinates that define the boundaries of the coral skeleton. Iso-surfaces were rendered with a threshold set to  $-190$  HU (additional details on the reconstruction procedure can be found in [39]). The resulting digital coral skeleton had an average surface roughness height of  $10 \pm 1.4$  mm and an average spacing of  $10 \pm 3.5$  mm, yielding a  $w/k$  ratio of approximately 1. All digital CAD files were converted to stereolithography (STL) file format for use in the large eddy simulation model, and also for 3D printing of physical models

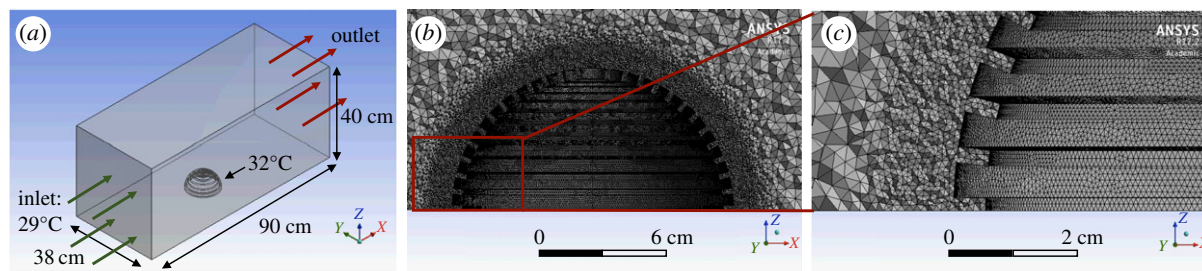


**Figure 3.** Numerical model domain set-up and boundary conditions. (a) Full model domain with inlet, outlet, and thermal boundary conditions, (b) close-up of discretized mesh in high-resolution box ( $\Delta x < 0.5$  cm) surrounding entire hemisphere model, (c) close-up of super high-resolution discretized mesh ( $\Delta x < 0.1$  cm) adjacent to surface to capture boundary layer dynamics and thermal flux.

(figure 2e) used in water tunnel testing for experimental validation of the LES model (full validation details are found in the electronic supplementary material).

## 2.5. Large eddy simulations

### 2.5.1. Domain set-up

Numerical modelling of flow and heat transfer over the three idealized surface topographies and the coral skeleton was implemented via LES of turbulent flow coupled to a convective thermal energy transport model. The model fluid domain measured  $90 \text{ cm} \times 38 \text{ cm} \times 40 \text{ cm}$  (matching the size of the water tunnel test section used for validation). Boundary conditions (BC) were prescribed as follows: (i) incoming flow velocities were defined at the left inlet wall, (ii) a zero-pressure opening was assigned at the right outlet wall, (iii) adiabatic, no-slip BCs were set for the near and far walls and bottom, and (iv) an adiabatic free-slip BC was set for the domain top (figure 3a). The surface of each coral model was assigned a no-slip BC and a fixed temperature of  $32^\circ\text{C}$ , while the bulk fluid temperature was initialized at  $29^\circ\text{C}$ .

Each morphology was investigated for four flow conditions: unidirectional low ( $5 \text{ cm s}^{-1}$ ) and high ( $15 \text{ cm s}^{-1}$ ) flow, and oscillatory low and high flow with a wave period of 5 s, a timescale typical of coral habitats. To produce matching Reynolds numbers for the unidirectional and oscillatory cases, root-mean-square velocities (rms) for low and high flows were matched across the steady and unsteady regimes, which also allowed for total fluid motion within a given time period to be equal. The fluid domain was discretized using tetrahedral elements into three regions of increasing mesh density, with an outer flow maximum element size of 3.2 cm, a high-resolution box surrounding the coral model to capture wake structure with a maximum size of 0.5 cm, and a super high-resolution concentric sphere covering the nearest 1 cm boundary layer with a maximum size of 0.1 cm (figure 3b,c). Mesh quality was assessed using mean element skewness and orthogonal quality, with limiting criteria set to less than 0.5 and greater than 0.7, respectively. The full list of investigation parameters for the 16 model runs is given in table 1.

### 2.5.2. Governing equations and subgrid-scale model

The LES governing equations solved in the numerical model are the filtered Navier–Stokes momentum and continuity equations given, respectively, in tensor notation as:

$$\frac{\partial \bar{u}_i}{\partial t} + \frac{\partial}{\partial x_j} (\bar{u}_i \bar{u}_j) = -\frac{1}{\rho} \frac{\partial \bar{p}}{\partial x_i} + \nu \left( \frac{\partial^2 \bar{u}_i}{\partial x_j \partial x_j} \right) - \frac{\partial \tau_{ij}}{\partial x_j} \quad (2.1)$$

and

$$\frac{\partial \bar{u}_i}{\partial x_j} = 0, \quad (2.2)$$

where  $\rho$  is fluid density,  $p$  is pressure and  $\tau_{ij}$  is the subgrid-scale stress tensor, which requires modelling for closure. The overbars

in equations (2.1) and (2.2) represent filtered quantities, i.e. the resolved components of the full Navier–Stokes equations that are solved directly at grid points, while the remaining residual (or subgrid-scale) components are modelled. The subgrid-scale (SGS) stress tensor is modelled using a wall-adapted local eddy (WALE) viscosity  $\nu_T$  according to:

$$\tau_{ij} = -\nu_T \left( \frac{\partial \bar{u}_i}{\partial x_j} + \frac{\partial \bar{u}_j}{\partial x_i} \right), \quad (2.3)$$

where  $\nu_T$  is specified explicitly using a WALE model constant  $C_w = 0.5$ , the subgrid characteristic length scale  $\Delta x$ , and the filtered strain rate tensor  $\bar{S}_{ij}$  [40].

Simulation of heat flux is accomplished by coupling a thermal energy transport model to the LES momentum equations, where the filtered internal energy equation, represented by temperature  $T$ , is given by:

$$\frac{\partial \bar{T}}{\partial t} + \frac{\partial (\bar{u}_j \bar{T})}{\partial x_j} = \frac{\partial}{\partial x_j} \left( \mu \frac{\partial \bar{T}}{\partial x_j} - \overline{u'_j T'} \right), \quad (2.4)$$

where  $\overline{u'_j T'}$  is the heat flux term (prime notation here indicate residual terms). To achieve closure of the modelled heat flux, we specify a turbulent Prandtl number ( $Pr_t = 0.9$ ), which relates the heat eddy diffusivity,  $\epsilon_H = \overline{u'_j T'} / (\partial \bar{T} / \partial x_j)$ , to the SGS eddy viscosity from equation (2.3). The near-wall temperature gradient  $\partial \bar{T} / \partial x_j$  is then used with a model constant  $C_\mu = 0.9$  and the turbulent kinetic energy to calculate wall heat flux  $q_w$ . Additional details on the automatic wall heat function are found in [41].

Governing equations for flow and heat transfer were solved using ANSYS CFX 17.1 (ANSYS, Inc.; Canonsburg, PA). Advection terms in the momentum equation were treated with a bounded central differencing scheme, and transient terms were solved with an implicit second-order backward Euler method. Solution time step  $\Delta t$  was adjusted for each run based on peak flow velocity  $u_{\max}$  and smallest grid size  $\Delta x_{\min}$  to maintain a Courant–Friedrichs–Lewy (CFL) condition of approximately 1, i.e.  $(u_{\max} \Delta t) / \Delta x_{\min} \leq 1$ . Each simulation had a total run time of 60 s, with averaging of flow and heat parameters occurring over the final 30 s to allow for flow development and convergence of turbulence statistics.

### 2.5.3. Characterization of turbulent structures

Organized turbulent motions have been shown to be major drivers of heat and mass flux [42], and the intensity and structure of these features can be described in a number of ways. We chose to use the so-called  $Q$ -criterion, which identifies eddy vortex cores by locating fluid regions in which local rotation dominates local strain, and is defined as the second invariant of the velocity gradient tensor  $Q = -(1/2)(\partial u_i / \partial x_j)(\partial u_j / \partial x_i)$ . Where  $Q > 0$ , the vorticity tensor exceeds the rate of strain tensor, which identifies a coherent turbulent structure (unlike vorticity alone which, for example, can be large in parallel shear flows lacking turbulent eddies) [43]. To quantify the intensity of turbulence generated by each surface morphology, non-negative  $Q$ -criterion values at

**Table 1.** Summary of flow and computation parameters used in LES model runs.

run	morphology	flow regime	$u_{\infty,rms}$ ( $\text{cm s}^{-1}$ )	mesh elements	$\Delta t$ (s)	$Re$	$KC$ number	frequency parameter
1	smooth	unidirectional	5	1 427 023	0.040	6750	—	—
2	smooth	unidirectional	15	1 427 023	0.013	20 250	—	—
3	smooth	oscillatory	5	1 429 259	0.028	6750	2.6	4091
4	smooth	oscillatory	15	1 429 259	0.009	20 250	7.9	4091
5	$w/k = 0.5$	unidirectional	5	5 349 661	0.020	6750	—	—
6	$w/k = 0.5$	unidirectional	15	5 349 661	0.007	20 250	—	—
7	$w/k = 0.5$	oscillatory	5	5 269 693	0.028	6750	2.6	4091
8	$w/k = 0.5$	oscillatory	15	5 269 693	0.009	20 250	7.9	4091
9	$w/k = 2.0$	unidirectional	5	5 643 656	0.020	6750	—	—
10	$w/k = 2.0$	unidirectional	15	5 643 656	0.007	20 250	—	—
11	$w/k = 2.0$	oscillatory	5	5 643 819	0.028	6750	2.6	4091
12	$w/k = 2.0$	oscillatory	15	5 643 819	0.009	20 250	7.9	4091
13	coral	unidirectional	5	9 208 147	0.020	6750	—	—
14	coral	unidirectional	15	9 208 147	0.007	20 250	—	—
15	coral	oscillatory	5	9 261 241	0.028	6750	2.6	4091
16	coral	oscillatory	15	9 261 241	0.009	20 250	7.9	4091

a fixed point (approximately 0.25 cm above the midpoint of each hemisphere, indicated by the cross in figure 8a) were averaged over a 15 s window ( $30 \text{ s} < t < 45 \text{ s}$ ) for the high Reynolds number unidirectional and oscillatory conditions.

### 3. Results

#### 3.1. Mean and turbulence flow characteristics over *in situ* corals

The ranges of flow conditions during field data collection are shown in table 2. For all major parameters—i.e. total root-mean-square (rms) velocity, current and wave velocities, and wave periods—significant overlap occurs, indicating similar flow regimes were present across the three coral species. Coral diameters are larger than particle excursion lengths for nearly all records, resulting in  $KC$  numbers less than 1.0. Using the crest of the roughness elements as the measurement datum, boundary layer profiles of rms horizontal velocity are shown in figure 4a for each coral species. To compare across varying flow conditions, profiles are normalized by the ‘local’ free-stream rms velocity  $u_{\infty,rms}$ , which accounts for both current and wave forcing and is calculated as the mean of the top 1 cm of measurement bins, approximately 2–3 cm above the surface. *Siderastrea siderea* and *D. labyrinthiformis*—the smooth and *d*-type corals, respectively—exhibit nearly identical vertical profiles with a steep gradient near the coral surface, typical of a wall-bounded shear layer. The profile of the *k*-type *C. natans* coral shows a region of strong local velocity enhancement, up to 75% greater than  $u_{\infty,rms}$  extending from approximately  $z = 0.5 \text{ mm}$  to  $z = 1.5 \text{ mm}$ . This accelerated flow is likely due to the injection of high-momentum vortices

out of the roughness cavity into the boundary layer and is also seen in the profiles of turbulence parameters (figure 4b,c).

Peaks in Reynolds shear stress occur at approximately the same vertical location above the surface, i.e.  $z = 0.5 \text{ mm}$ , for all coral types; however, the magnitude of  $\overline{u'w'}$  for the *k*-type coral is approximately  $2\times$  larger than either the smooth or *d*-type coral (figure 4b). An even larger enhancement of greater than 500% for *C. natans* is seen in normalized turbulent kinetic energy  $TKE$ , which remains elevated throughout the water column height (figure 4c). For each coral species, normalized bed shear stress levels calculated from the combined wave-current formulation described above compare well to direct Reynolds stress estimates, given by  $\tau_b = -\rho \overline{u'w'}$  (figure 5). The *k*-type *C. natans* coral shows a  $2\times$  and  $4\times$  enhancement in  $\tau_b$  relative to the smooth *S. siderea* and *d*-type *D. labyrinthiformis* corals, respectively. Differences in average  $\tau_b$  between each species are all significant at the  $p < 0.05$  level (Welch’s *t* test: *C. natans* by *S. Siderea*,  $t = 1.9$ , d.f. = 20; *C. natans* by *D. labyrinthiformis*,  $t = 3.5$ , d.f. = 15; *S. siderea* by *D. labyrinthiformis*,  $t = 2.7$ , d.f. = 8).

#### 3.2. Large eddy simulation numerical model results

##### 3.2.1. Mean velocity fields and surface shear stresses

Fluid advection most directly influences interfacial heat flux through mean velocity gradients and turbulence characteristics along the coral surface. Thus, in figure 6 we show cross-sections of mean streamwise velocity—extracted from the domain midplane—combined with contours of mean surface shear stress for all four surface morphologies under high Reynolds number unidirectional flow. For clarity, the other flow cases are omitted, particularly as the patterns of flow

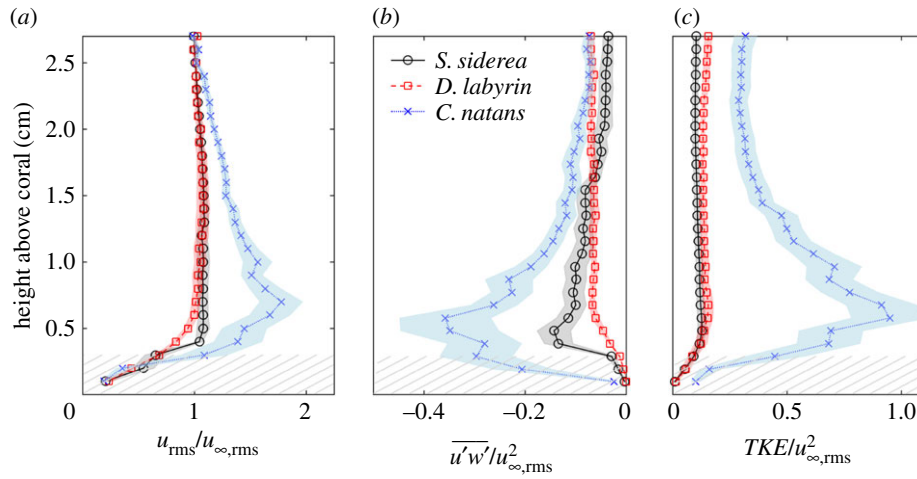


**Figure 4.** Vertical profiles of mean and turbulent flow parameters over *in situ* corals. (a) Normalized rms horizontal velocity  $u_{\text{rms}}$ , (b) normalized mean Reynolds shear stress  $\overline{u'w'}$ , (c) normalized turbulent kinetic energy  $TKE$ . Shaded colour regions indicate  $\pm 1$  standard error of the mean (s.e.m.). Grey hatching indicates region of less reliable data due to interference from acoustic reflections.

**Table 2.** Summary of morphological dimensions of *in situ* corals and ranges (min–max) of wave-current flow characteristics measured over Panamanian reef corals.

	roughness ratio	coral diameter	RMS horizontal velocity	mean current velocity	maximum wave orbital velocity	mean wave period	$KC$ number	frequency parameter
species	$w/k$ (–)	$L$ (cm)	$u_{\infty,\text{rms}}$ ( $\text{cm s}^{-1}$ )	$u_{\infty,c}$ ( $\text{cm s}^{-1}$ )	$u_{\text{om}}$ ( $\text{cm s}^{-1}$ )	$T$ (s)	$KC$ (–)	$\beta$ ( $\times 10^4$ )
<i>S. siderea</i>	—	25	1.4–4.3	0.3–1.9	3.0–13.8	2.0–3.7	0.3–1.3	1.9–3.5
<i>D. labyrinth</i>	$\sim 0.8$	28	1.5–5.9	0.2–1.6	1.2–5.8	1.5–3.0	0.1–0.3	2.9–5.7
<i>C. natans</i>	$\sim 1.2$	39	0.7–3.3	0.2–1.6	0.7–5.6	1.8–3.9	0.1–0.3	4.4–9.6

features are similar across test regimes. In figure 6, we note two key features impacting heat transfer: first, the steepest near-surface velocity gradients occur along the leading edge for each morphology, just upstream of flow separation resulting from the trailing edge adverse pressure gradient. The oscillatory condition (not shown) exhibits similar patterns but occurring on both sides of the coral models due to the flow reversal. Locations of greatest surface shear stresses correspond to regions of steepest velocity gradients and increase in magnitude at higher  $Re$  number. These locations of high shear are particularly evident at the most exposed tips of the roughness elements. Second, close inspection of the roughness cavities shows vortical motion penetrating fully to the bottom of the  $k$ -type roughness and coral skeleton (figure 6*c,d*); whereas, for the  $d$ -type roughness, the lid-driven flow reaches only approximately half the cavity depth (figure 6*b*).

To quantify the fluid motion within roughness elements, vertical profiles of intra-cavity velocities were extracted from within the roughness cavity located at a polar angle of  $45^\circ$  from the leading edge and extending normal from the cavity bottom for approximately 2.5 cm (illustrated by the dashed line in figure 6*c*). Under unidirectional flows (figure 7), the  $k$ -type roughness exhibits vortical flows with magnitudes greater than 50% of free-stream velocity penetrating fully to the cavity bottom. The  $d$ -type roughness, by contrast, shows a peak vortical flow magnitude less than 10% of free-stream velocity and negligible flow within the bottom third of the

cavity. For oscillatory flows (figure 7), the recirculation strength within  $k$ -type roughness is significantly reduced—by approximately 60% and 25% for low and high  $Re$ , respectively—however, the shape and magnitude of flow within the  $d$ -type cavities are largely unchanged.

### 3.2.2. Turbulence structure and intensity

Figure 8 shows iso-surfaces of  $Q$ -criterion ( $Q = 5 \text{ s}^{-2}$ ), combined with surface contours of mean wall heat flux, for each morphology under oscillatory high Reynolds number flow. The oscillatory regime inherently generates time-varying turbulence, and the iso-surfaces in figure 8 are shown at  $t = 45 \text{ s}$ , when streamwise velocity is at a maximum. The downstream turbulent wake structures identified by the iso-surfaces show increasing complexity and spatial distribution as the surface morphology increases in roughness. Additionally, the  $k$ -type morphology and coral skeleton produce significant turbulent structures along the leading edges.

Figure 9 shows the time-averaged intensity of the turbulent structures, demonstrating that the oscillatory flow generates between  $2$ – $4\times$  greater intensity, depending on morphology type, compared with equivalent unidirectional flow speeds. Additionally, turbulence production is enhanced as surface roughness increases, though at different rates for unidirectional and oscillatory regimes. Though the roughness spacing of the coral skeleton is approximately  $w/k \sim 1$ , i.e. between the  $d$ -type and  $k$ -type spacing, the irregular distribution of the

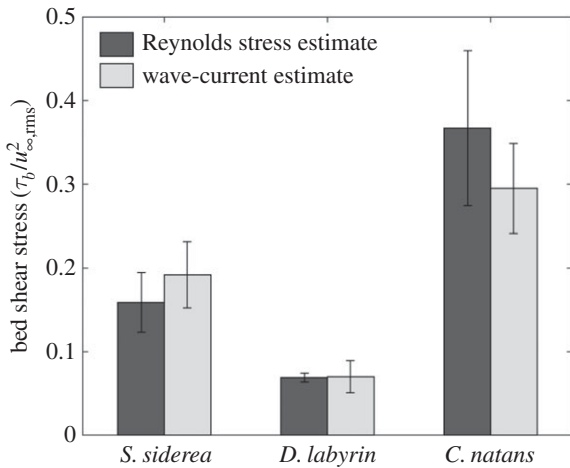


**Figure 5.** Normalized bed shear stresses  $\tau_b$  ( $\pm 1$  s.e.m.) for *in situ* corals. Values for *D. labyrinthiformis* and *C. natans* are reported for stresses at top of roughness elements.

roughness elements produces significantly larger and more intense turbulent structures (between 4–11 $\times$ ) compared with the idealized models.

### 3.2.3. Interfacial heat flux distributions and magnitudes

Patterns of interfacial heat flux  $q$  shown in figure 8 for oscillatory flow are largely consistent with the distribution of surface shear stresses shown in figure 6 for unidirectional flow. The key difference is that the heat transfer occurs symmetrically on both sides of the coral models under oscillatory flow, with locations of peak transfer rates remaining primarily on the most exposed tips of the roughness elements. Quantitative values of mean (with respect to surface area and time) wall heat flux  $\bar{q}_w$  are given in table 3 for all 16 model runs. The oscillatory conditions produce a 1.2–2 $\times$  increase in mean heat flux compared with equivalent unidirectional flow, while an increase in Reynolds number generates a 2–3.3 $\times$  enhancement in  $\bar{q}_w$ , depending on surface geometry. Non-negligible heat flux is also found in areas of minimal wall shear, for example, in regions downstream of flow separation where near-surface velocity gradients are small. Since the numerical model explicitly calculates heat flux using near-surface turbulent kinetic energy and boundary layer temperature profiles (see equation (2.4)) rather than using wall shear stresses, physically realistic convective heat transfer is still captured in these regions.

Greater surface roughness, as defined by a larger  $w/k$  ratio, produces up to a 2 $\times$  increase in  $\bar{q}_w$ , though with two notable exceptions. First, at low  $Re$ , unidirectional flow, the *d*-type roughness actually exhibits a smaller mean wall heat flux compared with the smooth model, likely due to the limited intra-cavity flow, which acts to reduce the amount of surface area on the leading edge exposed to high shear flow. Second, the coral skeleton always exhibits enhanced heat flux compared with the other models—a result of its highly irregular distribution of roughness elements compared with the simplified morphology of the idealized models. The differences in morphology make it important to account for differences in surface area by examining total wall heat flux  $q_{\text{tot}}$  (table 3).  $q_{\text{tot}}$  captures trade-offs inherent in the ability of large roughness to enhance turbulence production and turbulence-mediated heat transfer (as exemplified by the *k*-type roughness) versus the greater available surface area

of dense roughness (as exemplified by the approximately 50% larger surface area for the *d*-type roughness). Values of  $q_{\text{tot}}$  show that despite the larger surface area of the *d*-type morphology, the turbulence-enhanced heat transfer of the *k*-type morphology generates between 5–35% more total heat transfer for most conditions. However, under high Reynolds number oscillatory flow, the extra surface area of the *d*-type morphology, in conjunction with turbulence intensity levels approaching that of the *k*-type morphology (figure 9), generates the largest total heat flux of all flow–morphology combinations, with the exception of the coral skeleton. This indicates that the local flow–structure interaction has shifted the trade-offs that drive enhancements in scalar flux.

### 3.2.4. Time series of a half-wave cycle

To best illustrate the distinct physical mechanisms driving convective heat transfer for the *d*-type surface morphology under oscillatory high- $Re$  flow, we show individual time-steps of key flow and temperature parameters through a half-wave cycle in figure 10. At  $t = 0$ , the mean free-stream flow is from left-to-right at its maximum of 21.2 cm s $^{-1}$ , and the pressure field resembles typical unidirectional flow with a high-pressure peak at the leading-edge stagnation point and a low-pressure region in the area of flow separation. Iso-surfaces of temperature ( $T = 29.5^\circ\text{C}$ ) and  $Q$ -criterion ( $Q = 5 \text{ s}^{-2}$ ) show a long tail of high temperature flow downstream and a region of turbulent activity attached to the coral's trailing edge with coherent structures shed in the wake flow. As the wave-induced pressure field begins to reverse the free-stream potential flow from  $t = \pi/3$  to  $t = 2\pi/3$ , the high-temperature and high-vorticity regions migrate along the surface of the coral from right-to-left. The crucial mechanism in the wave cycle occurs from  $t = 2\pi/3$  to  $t = \pi$  when the very large low-pressure field (on left of panel) acts not only to advect the previously shed high-temperature fluid, but importantly, also to suction out additional high-temperature fluid from the large surface area on the coral's left side (note the large volume of high-temperature fluid attached to the coral surface at  $t = 2\pi/3$ ). Turbulent vortices then advect down the coral surface, pinching off and pushing a large slug of high-temperature fluid away from the coral.

## 4. Discussion

### 4.1. Implications of field data

In the Panamanian reef, we measured significantly larger near-surface turbulence characteristics and bed shear stresses for the *k*-type *C. natans* corals compared with the smooth *S. siderea* or *d*-type *D. labyrinthiformis* corals, which would suggest a corresponding enhancement in rates of heat and mass flux. A meta-analysis of previous field and laboratory data found mass transfer rates correlate highly ( $r^2 > 0.9$ ) with bed shear stress according to  $q_m \propto \tau_b^{0.4}$  for both wave and current-only flows [22]. For the bed stress values measured here, this scaling would imply mass transfer rates for *C. natans* that are approximately 86% higher than *D. labyrinthiformis* and approximately 29% higher than *S. siderea*. However, the proposed correlations are derived primarily from reef-scale O(10–100 s m) studies of nutrient uptake that use an area-integrated approach to estimating mass flux, thereby eliminating the heterogeneous

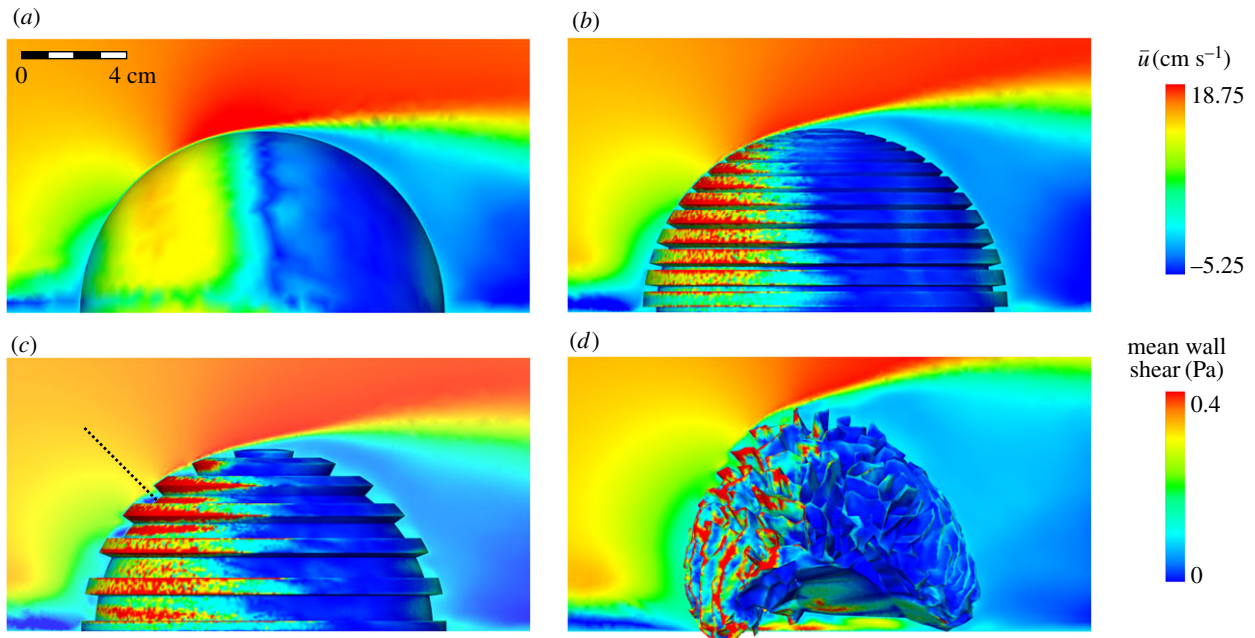


**Figure 6.** Mid-plane transects of mean streamwise velocity  $\bar{u}$  and surface contours of mean wall shear for high Reynolds number ( $Re = 20\,250$ ) unidirectional flow test case. (a) Smooth morphology, (b) *d*-type roughness morphology, (c) *k*-type roughness morphology, (d) coral skeleton. Dashed line in (c) indicates location of intra-cavity vertical profiles shown in figure 7.

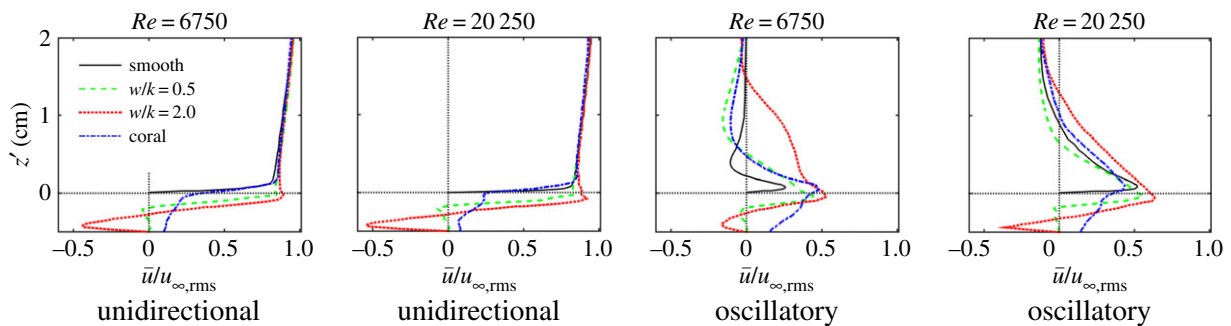


**Figure 7.** Surface-normal ( $z'$ ) profiles of mean streamwise velocity (normalized by rms free-stream velocity  $u_{\infty,rms}$ ) for all 16 simulation test cases. Data are extracted from the mid-plane transect at a leading-edge polar angle of  $45^\circ$ , beginning at bottom of roughness cavity and extending outward perpendicular to surface. Intra-cavity regions are indicated by  $z' < 0$ .

spatial effects of coral-scale roughness features on mass-momentum transfer relationships. These relationships lack theoretical justification at the individual coral-scale and likely do not hold, especially as spatial variability has been shown to play an important role in nutrient uptake and structural remodelling as seen in field [34], laboratory [44], and numerical simulation studies [45]. As it is unlikely the species studied here genuinely experience such large differences in rates of heat and mass transfer as implied by the reef-scale relationships, the hydrodynamic data suggests a more complex mass-momentum relationship exists and depends on other physical mechanisms. Accordingly, Falter *et al.* [22] propose that the greatest uncertainty in predicting community scale mass transfer rates 'will likely stem from spatial heterogeneity in the size and distribution of roughness features as well as in the amount of added surface area these features provide'.

The low  $KC$  numbers measured *in situ*, coupled with the large frequency parameters  $\beta$ , indicate the coral-scale flow is close to the critical transition from unseparated flow to the onset of vortical instabilities [25]. In this  $KC$  range, inertial flow effects dominate relative to the large drag forces present

at higher  $KC$  (e.g. for long-period waves or unidirectional flow), suggesting that flow conditions play an important role in determining which physical mechanisms of turbulence-mediated heat and mass transfer are present, beyond bed shear stress alone. Further, the measurements here were taken only at a single location on top of a roughness element near the crest of the coral. The modelling results show flows within roughness cavities (figure 7) exhibit significantly smaller vertical gradients and reduced surface shear, consistent with previous data for branching corals [21] and flat-plate 2D bar roughness [46]. Increasing the density of surface roughness offers a potential solution to the common biological goal of maximizing surface area for a given volume, but at the expense of reducing turbulence production, a trade-off whose impacts on heat and mass exchange depend on local hydrodynamic conditions at both the  $O(m)$  coral scale and the  $O(cm)$  roughness element scale. This suggests point measurements (and extrapolated correlations) are unable to provide realistic estimates of complex variations in surface stresses and local heat and mass transfer rates.

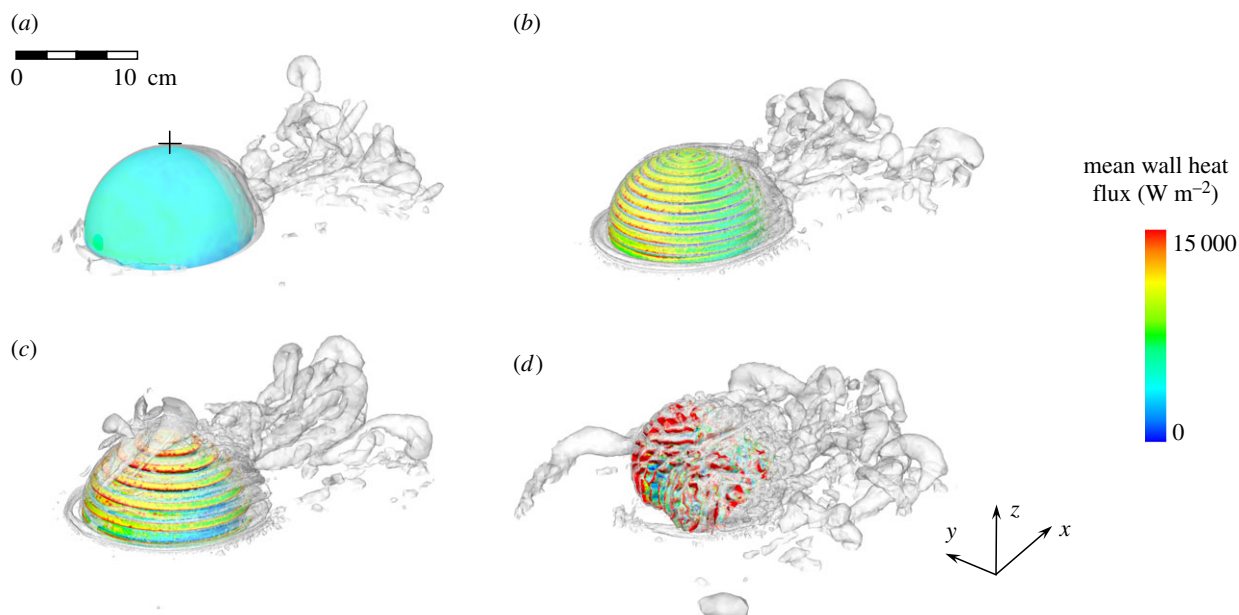


**Figure 8.** Surface contours of mean wall heat flux and iso-surfaces of  $Q$ -criterion ( $Q = 5 \text{ s}^{-2}$ ) for high Reynolds number ( $Re = 20\,250$ ) oscillatory flow test case. (a) Smooth morphology, (b)  $d$ -type roughness morphology, (c)  $k$ -type roughness morphology, (d) coral skeleton. Instantaneous  $Q$ -criterion data taken at  $t = 45 \text{ s}$ , when streamwise velocity is at a maximum. Black cross in (a) indicates location of time-averaging of  $Q$ -criterion shown in figure 9.

## 4.2. Physical mechanisms optimizing trade-offs in heat transfer

To simplify the complex surface morphology of corals, we used an idealized engineering analogue, i.e. two-dimensional bar roughness, which has been shown to exhibit maximum heat transfer for a roughness spacing-to-height ratio  $w/k$  of approximately 7–8 for flat plates under unidirectional flow [47]. At this spacing, form drag from individual roughness elements is maximized—both in absolute terms and also relative to skin friction drag, which can be considered essentially a normalized wall shear stress, i.e.  $C_f = \tau_b / (0.5\rho u_\infty^2)$ . Additionally, for this  $w/k$  range, wall-normal turbulent fluctuations, i.e. those responsible for vertical flux, are at their strongest [46]. These findings further reinforce that the mass-momentum correlations described above based on bed shear stress at the reef-scale do not apply at the roughness element scale, where local form drag plays a dominant role. However, such high  $w/k$  roughness ratios are not typically seen among coral morphologies, suggesting other factors influence the optimization of trade-offs, such as the hemispheric shape of the coral or the oscillatory flow conditions to which corals are typically exposed where  $KC$  is usually less than 10 (compared with an effectively infinite  $KC$  number for unidirectional flow). Our simulation results for total heat flux demonstrate that a much smaller  $w/k$  ratio of 0.5—representative of  $d$ -type roughness—can outperform the heat transfer capabilities of turbulence-enhancing  $k$ -type roughness under specific flow conditions, in particular, high Reynolds number oscillatory flow. This suggests that for hemispheres exposed to unsteady flow, the underlying physical mechanisms responsible for optimizing interfacial scalar flux differ from that for flat plate roughness, in which maximizing drag is the key factor.

The  $KC$  number for the oscillatory high- $Re$  regime ( $KC = 7.9$ ) falls directly within the range of  $KC$  numbers (roughly  $7 < KC < 9$ ) in which drag and inertia coefficients,  $C_d$  and  $C_{mv}$ , respectively, have been shown to balance each other across a range of frequency parameters and surface roughnesses [25]. At smaller  $KC$ , inertia forces dominate, leading to

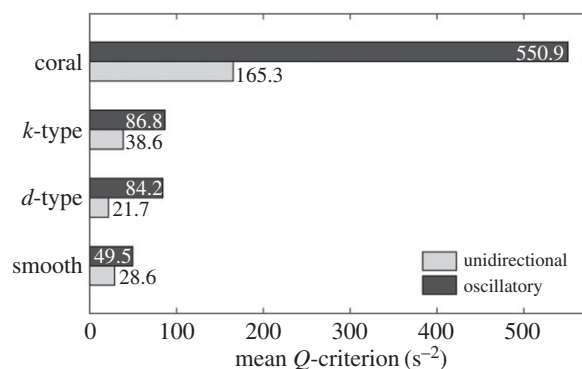


**Figure 9.** Time averages of  $Q$ -criterion values located at point indicated by cross in figure 8a. Averages were computed for 15 s range between  $30 \text{ s} < t < 45 \text{ s}$  for unidirectional and oscillatory high Reynolds number test cases.

fluid accelerations and inducing ‘suction’; while for larger  $KC$ , drag forces dominate, leading to vortex shedding and advection. The half-wave cycle shown in figure 10 demonstrates that both mechanisms are critical components in maximizing heat transfer. This force balance likely plays a key role in determining the optimal trade-off between surface area and turbulence production across roughness morphologies. Under most flow conditions tested here, the  $k$ -type surface morphology generates significantly more intense turbulent vortices (as indicated by the larger mean  $Q$ -criterion), while possessing approximately 28% less surface area than the  $d$ -type morphology (table 3). However, under oscillatory high- $Re$  forcing, the average vortex intensity of the  $d$ -type morphology nearly approaches that of the  $k$ -type (and nearly double the smooth morphology), while the extra surface area enables a greater total heat flux, even if the flow does not fully penetrate the roughness cavities as seen in figure 7.

Additionally, the  $KC$  number also determines the type of vortex regime generated. Following the framework established by Tatsuno & Bearman [24], a small  $KC$  (on the order of 2.5) is typically characterized by vortex formation from instabilities in the boundary layer; whereas, a high  $KC$

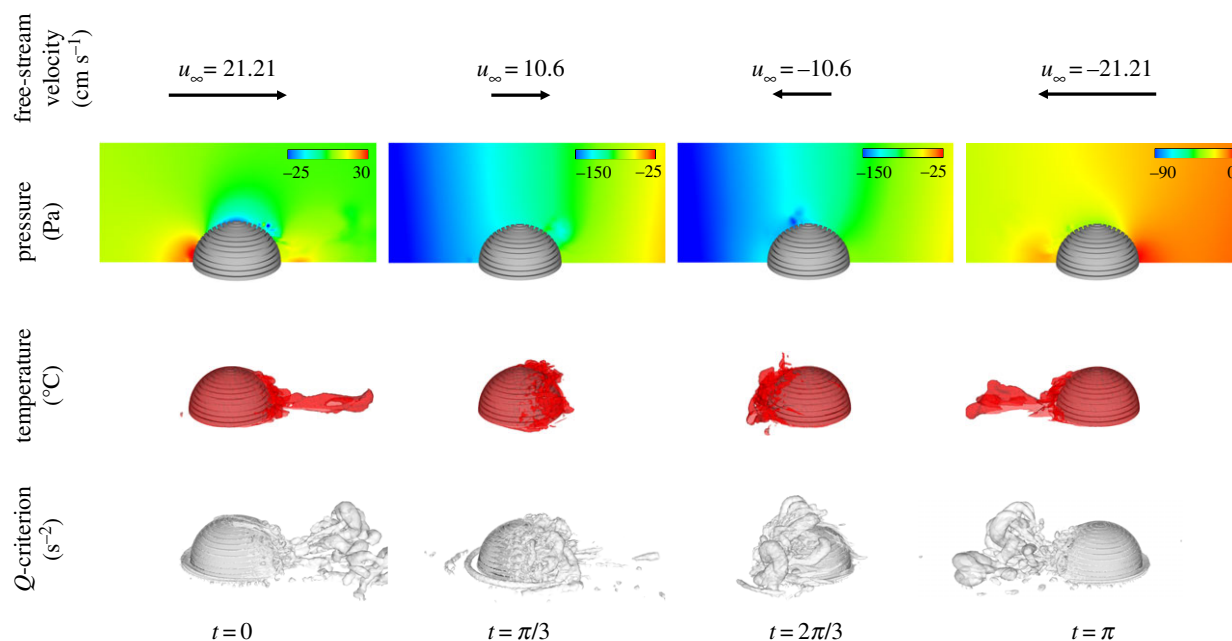


**Figure 10.** Time series of a half-wave cycle ( $0 \leq t \leq \pi$ ) of high Reynolds number oscillatory flow past  $d$ -type surface roughness. (Top row) Instantaneous free-stream horizontal velocity  $u_\infty$ , (second row) mid-plane transcepts of pressure fields (note the changing scale at each time step), (third row) iso-surfaces of high-temperature fluid ( $T = 29.5^\circ\text{C}$ ) shed from coral model surface, (bottom row) eddy vortex cores identified by iso-surfaces of  $Q$ -criterion ( $Q = 5 \text{ s}^{-2}$ ).

**Table 3.** Summary of LES model results for mean wall heat flux  $\bar{q}_w$  (with respect to surface area and time), total interfacial heat flux  $q_{\text{tot}}$ , and equivalent mass transfer coefficient  $\bar{h}_m$  using diffusion coefficient for dissolved  $\text{NH}_4^+$  as example.

flow regime	$u_{\infty, \text{rms}}$ ( $\text{cm s}^{-1}$ )	smooth	$d$ -type	$k$ -type	coral
<i>mean wall heat flux, <math>\bar{q}_w \times 10^3</math> (<math>\text{W m}^{-2}</math>)</i>					
unidirectional	5	1.78	1.32	2.14	2.58
oscillatory	5	1.77	1.94	3.71	5.18
unidirectional	15	3.51	3.79	5.50	6.63
oscillatory	15	4.18	6.41	8.84	10.37
<i>total wall heat flux, <math>q_{\text{tot}} \times 10^2</math> (W)</i>					
unidirectional	5	0.51	0.81	0.95	2.05
oscillatory	5	0.51	1.20	1.64	4.11
unidirectional	15	1.00	2.33	2.43	5.27
oscillatory	15	1.20	3.95	3.91	8.24
<i>mean mass transfer coefficient for <math>\text{NH}_4^+</math>, <math>\bar{h}_m \times 10^{-6}</math> (<math>\text{m s}^{-1}</math>)</i>					
unidirectional	5	7.58	5.65	9.12	11.05
oscillatory	5	7.58	8.35	15.93	22.23
unidirectional	15	15.03	16.19	23.52	28.40
oscillatory	15	17.86	27.50	37.91	44.46
<i>total surface area (<math>\text{cm}^2</math>)</i>		286.0	615.8	442.2	794.5

(greater than  $\sim 6$ ) is characterized by a vortex street generated by flow separation against an adverse pressure gradient. As such, the distinct structure and dynamics of the vortices produced by different  $KC$  regimes likely play an important role in the different rates of convective heat transfer generated by these coherent turbulent motions. Thus, as  $C_d$  and  $C_m$  vary within  $KC$  regimes, the amount and intensity of turbulence production and the relative influence of drag and inertia forces will shift the

optimal trade-off between turbulence-mediated shear/advection and available surface area that maximizes scalar flux.

### 4.3. Extension to coral mass transfer

Though the numerical model simulated only convective heat transfer, mass transfer parameters can be quantified through the heat-mass transfer analogy, which relates Nusselt number (the dimensionless ratio of convective to conductive

heat transfer) and Sherwood number (the dimensionless ratio of convective to diffusive mass transfer). Heat and mass transfer coefficients are related according to the relationship:

$$\frac{h}{h_m} = \frac{k}{D[k/(\rho c_p D)]^{1/3}}, \quad (4.1)$$

where  $k$  is the fluid thermal conductivity,  $D$  is the diffusion coefficient of the mass scalar of interest and  $c_p$  is the specific heat capacity of the fluid [48]. Corals are typically mass-transfer limited, i.e. subject to kinetic control of scalar exchange, and therefore, this heat–mass transfer analogy is valid and can be applied to coral systems. However, for corals located in heavily nutrient-rich environments where uptake can be limited by the rate of biological usage, equation (4.1) may no longer be applicable. Using ammonium  $\text{NH}_4^+$  as an example nutrient of interest ( $D = 1.8 \times 10^{-9} \text{ m}^2 \text{ s}^{-1}$ ) [49], equivalent mean mass transfer coefficients  $\bar{h}_m$  for each surface geometry and flow regime are given in table 3. As expected from the heat–mass transfer analogy, the pattern of mass flux enhancement with respect to morphology and flow condition follows that of  $\bar{q}_w$ . When accounting for surface area to estimate total mass flux, the  $d$ -type morphology again outperforms the  $k$ -type morphology under oscillatory high Reynolds number flow.

The converted mass transfer coefficients found here are smaller—though of the same relative order of magnitude—than previously reported reef-scale nutrient uptake constants obtained using direct measurements in an enclosed biome ( $54\text{--}126 \times 10^{-6} \text{ m s}^{-1}$ ) [3] or estimates from frictional dissipation across a reef flat ( $57\text{--}185 \times 10^{-6} \text{ m s}^{-1}$ ) [16]. Though the coral skeleton under oscillatory high- $Re$  flow approaches these uptake rates (approx.  $44 \times 10^{-6} \text{ m s}^{-1}$ ), the underestimates are likely due to greater turbulence production from the reef-scale morphological complexity and from the additional presence of a background mean flow component, which has been shown to enhance near-bed mass transport [50]. At the coral-scale, the numerical results here are consistent with field and laboratory measurements of mass flux estimated from dissolution of plaster forms, ranging from  $5.8\text{--}34.7 \times 10^{-6} \text{ m s}^{-1}$  [15]. This previous work, however, demonstrated a linear relationship between the total surface area and mass transfer coefficients for a variety of smooth and rough forms, which was thought to occur because all the roughness scales studied exceeded the CBL thickness and all surfaces experienced comparable flow conditions. While such conditions may have been met in prior experimental designs, the numerical model here clearly demonstrates that significant spatial heterogeneity in flow conditions is present for all surface morphologies and that the relationship between  $\bar{h}_m$  and surface area is only one component of the complicated fluid–structure interaction that determines scalar flux, including turbulence production, vortex type, and the ratio of inertia and drag forces.

#### 4.4. Limits of the numerical model

The numerical model here offers valuable insights into the complex physics controlling interfacial flux, but several limitations constrain the degree to which it can be extrapolated and suggest avenues for future investigations. Only two  $w/k$  roughness ratios were investigated, whereas many other morphological features have been shown to impact near-surface hydrodynamics and mass flux, such as intermediate roughness ratios between  $d$ -type and  $k$ -type [27], triangle-shaped

roughness elements [51], and even surface ciliary action [52]. Additionally, only two  $KC$  numbers were investigated. The lower  $KC$  in this study resulted solely from a reduction in Reynolds number, but as  $KC$  is a function of flow speed, wave period, and object size, other variable changes, such as coral diameter or wave period, would also reduce the  $KC$  number to provide further insights into the dynamics of the fluid–structure interaction. Finally, the idealized surface morphologies are only strictly valid approximations of bar roughness along the midline and become less accurate near the lateral edges. This discrepancy is most clearly evident when comparing the idealized morphologies to the coral skeleton, whose highly convoluted surface generates between  $4\text{--}7\times$  greater vortex intensity (figure 9). The coral skeleton generates levels of near-surface shear stress that compare well to actual  $k$ -type corals measured in the field (data not shown) and produces mean convection coefficients that significantly outperform the idealized models under every flow regime investigated.

The model implemented here also assumes a uniformly heated coral surface, which is a simplification of the spatial variation of surface heating driven by solar irradiance. Evidence suggests that morphological features of a coral skeleton can act to scatter incident light, creating variability in patterns of solar absorption [53]. This scattering enhances the overall efficiency of energy collection for photosynthetic symbionts, but creates a potentially detrimental side effect of excessive heat retention. During periods of low flow and high irradiance, for example, the surface of massive corals was found to exceed the surrounding water temperature by up to  $0.6^\circ\text{C}$  [54]. When this heating from irradiance absorption is coupled with rising sea surface temperatures, thermal stress conditions intensify, further accelerating coral bleaching events. At the same time, however, our study suggests that these same morphological features may also enhance convection coefficients, thereby limiting the effects of surface heating caused by solar irradiance.

#### 4.5. Biological implications

Differential rates of mass transfer have profound effects on both intra-specific morphological plasticity and inter-specific competition. Local environmental gradients of nutrients that are typically controlled by hydrodynamic conditions have, for example, been shown to produce denser carbonate skeletons, increase zooxanthellae counts and improve reproductive output during exposure to fast flows [1]. In addition to nutrients, the flow-driven efflux of dissolved gasses such as  $\text{O}_2$  has been demonstrated to augment rates of coral photosynthesis [5]. Thus, morphological changes that function to enhance rates of mass flux, such as roughness element growth, can generate a positive feedback loop that promotes greater efficiency of mass transfer and additional growth. Further, exploitation of hydrodynamic niches within various flow environments has been shown to produce new morphological phenotypes (without speciation) that optimize heat and mass flux, resulting in particular size and species habitat distribution patterns [55]. For example, larger coral size was found to correlate with greater wave activity, i.e. larger wave heights and orbital velocities [56]. Such patterning is consistent with the findings presented here, where for example, a large coral length scale  $L$  and a large particle excursion length ( $U_{\text{max}}T$ ) can balance each other to generate  $KC$  numbers (i.e.  $KC = U_{\text{max}}T/L$ ) comparable to those of

smaller corals exposed to less active wave conditions, thereby maintaining the same underlying physical mechanisms that drive scalar flux.

Perhaps the single greatest threat to the future sustainability of corals is global warming due to anthropogenic climate change. The extreme marine heat wave of 2016, for example, resulted in a record loss of Great Barrier Reef corals and demonstrated how reef assemblages are transformed due to differential survivorship. In particular, temperature-sensitive species died almost immediately due to heat stress, while other coral species slowly starved due to the expulsion of nutrition-producing symbionts, which together resulted in an overall reduction in reef biodiversity and a regime shift from fast-growing branching coral species to newly dominant slow-growing corals with simple morphologies [57]. Hemispherical stony corals in particular have been shown to be less vulnerable to marine warming compared with branching corals [58]. As climate change is projected to intensify, regions of tropical coastal ocean that exceed coral-temperature thresholds are expected to expand, further threatening the diversity of coral reef assemblages [28]. Those corals best able to mitigate thermal stress through more efficient heat transfer should be expected to demonstrate preferential survivorship and faster recovery

following bleaching events. Our findings suggest that surface morphology creates trade-offs between available surface area and roughness-induced turbulence that alter convective heat and mass transfer rates. In addition, our work helps explain how variations in flow conditions, in particular oscillatory flows, can interact with specific morphologies to reduce the severity of heat-related coral stressors.

**Data accessibility.** Data are publicly available at the University of Virginia Dataverse repository, <https://doi.org/10.18130/V3/CS8ZQH>.

**Authors' contributions.** J.B.S. and M.A.R. designed the research and performed the field measurements. J.B.S. performed the computational simulations and analysed the data. R.S. and C.L. performed the 3D-reconstruction of the coral skeleton. J.B.S. wrote the manuscript with editorial assistance from M.A.R., R.S. and C.L. All authors gave final approval for publication.

**Competing interests.** We declare we have no competing interests.

**Funding.** We acknowledge funding from the U.S. National Science Foundation to M.A.R. (grant no. OCE-1151314).

**Acknowledgements.** We thank Ross Timmerman for assistance with Panama field data collection, and the Smithsonian Tropical Research Institute in Bocas del Toro, Panama for support with research facilities. We thank Heinrich Seilkopf and the Radiologie im Duererhof, Friedrich-Ebert-Str. 21, 95448 Bayreuth, Germany for provision of the CT scanner, and Immanuel Goerens for performing the CT scans.

## References

- Mass T, Brickner I, Hendy E, Genin A. 2011 Enduring physiological and reproductive benefits of enhanced flow for a stony coral. *Limnol. Oceanogr.* **56**, 2176–2188. (doi:10.4319/lo.2011.56.6.2176)
- Dennison WC, Barnes DJ. 1988 Effect of water motion on coral photosynthesis and calcification. *J. Exp. Mar. Biol. Ecol.* **115**, 67–77. (doi:10.1016/0022-0981(88)90190-6)
- Atkinson M, Falter J, Hearn C. 2001 Nutrient dynamics in the Biosphere 2 coral reef mesocosm: water velocity controls NH<sub>4</sub> and PO<sub>4</sub> uptake. *Coral Reefs* **20**, 341–346. (doi:10.1007/s00338-001-0184-7)
- Lesser MP, Weiss V, Patterson MR, Jokiel J. 1994 Effects of morphology and water flow on carbon delivery and productivity in the reef coral, *Pocillopora damicornis* (Linnaeus): diffusion barriers, inorganic carbon limitation, and biochemical plasticity. *J. Exp. Mar. Biol. Ecol.* **178**, 153–179. (doi:10.1016/0022-0981(94)90034-5)
- Mass T, Genin A, Shavit U, Grinstein M, Tchernov D. 2010 Flow enhances photosynthesis in marine benthic autotrophs by increasing the efflux of oxygen from the organism to the water. *Proc. Natl Acad. Sci. USA* **107**, 2527–2531. (doi:10.1073/pnas.0912348107)
- Reidenbach MA, Koseff JR, Koehl MAR. 2009 Hydrodynamic forces on larvae affect their settlement on coral reefs in turbulent, wave-driven flow. *Limnol. Oceanogr.* **54**, 318–330. (doi:10.4319/lo.2009.54.1.0318)
- Jimenez IM, Kuhl M, Larkum AWD, Ralph PJ. 2011 Effects of flow and colony morphology on the thermal boundary layer of corals. *J. R. Soc. Interface* **8**, 1785–1795. (doi:10.1098/rsif.2011.0144)
- Hondzo M. 1998 Dissolved oxygen transfer at the sediment–water interface in a turbulent flow. *Water Resour. Res.* **34**, 3525–3533. (doi:10.1029/1998WR900009)
- O'Connor BL, Hondzo M. 2008 Dissolved oxygen transfer to sediments by sweep and eject motions in aquatic environments. *Limnol. Oceanogr.* **53**, 566–578. (doi:10.4319/lo.2008.53.2.0566)
- Jørgensen BB, Des Marais DJ. 1990 The diffusive boundary layer of sediments: oxygen microgradients over a microbial mat. *Limnol. Oceanogr.* **35**, 1343–1355. (doi:10.4319/lo.1990.35.6.1343)
- T. Nakamura, R. van Woessik. 2001 Water-flow rates and passive diffusion partially explain differential survival of corals during the 1998 bleaching event. *Mar. Ecol. Prog. Ser.* **212**, 301–304. (doi:10.3354/meps212301)
- Lenihan HS, Adjeroud M, Kotchen MJ, Hench JL, Nakamura T. 2008 Reef structure regulates small-scale spatial variation in coral bleaching. *Mar. Ecol. Prog. Ser.* **370**, 127–141. (doi:10.3354/meps07622)
- Hooidonk R, Maynard JA, Manzello D, Planes S. 2013 Opposite latitudinal gradients in projected ocean acidification and bleaching impacts on coral reefs. *Glob. Change Biol.* **20**, 103–112. (doi:10.1111/gcb.12394)
- Atkinson MJ, Bilger RW. 1992 Effects of water velocity on phosphate uptake in coral reef-flat communities. *Limnol. Oceanogr.* **37**, 273–279. (doi:10.4319/lo.1992.37.2.0273)
- Falter JL, Atkinson MJ, Coimbra CF. 2005 Effects of surface roughness and oscillatory flow on the dissolution of plaster forms: evidence for nutrient mass transfer to coral reef communities. *Limnol. Oceanogr.* **50**, 246–254. (doi:10.4319/lo.2005.50.1.0246)
- Falter JL, Atkinson MJ, Merrifield MA. 2004 Mass-transfer limitation of nutrient uptake by a wave-dominated reef flat community. *Limnol. Oceanogr.* **49**, 1820–1831. (doi:10.4319/lo.2004.49.5.1820)
- Sebens KP, Witting J, Helmuth B. 1997 Effects of water flow and branch spacing on particle capture by the reef coral *Madracis mirabilis* (Duchassaing and Michelotti). *J. Exp. Mar. Biol. Ecol.* **211**, 1–28. (doi:10.1016/S0022-0981(96)02636-6)
- Storlazzi CD, Brown EK, Field ME, Rodgers K, Jokiel PL. 2005 A model for wave control on coral breakage and species distribution in the Hawaiian Islands. *Coral Reefs* **24**, 43–55. (doi:10.1007/s00338-004-0430-x)
- Lowe RJ, Koseff JR, Monismith SG, Falter JL. 2005 Oscillatory flow through submerged canopies: 2. Canopy mass transfer. *J. Geophys. Res.* **110**, C10017. (doi:10.1029/2004JC002789)
- Reidenbach MA, Koseff JR, Monismith SG. 2007 Laboratory experiments of fine-scale mixing and mass transport within a coral canopy. *Phys. Fluids* **19**, 075107. (doi:10.1063/1.2752189)
- Reidenbach MA, Koseff JR, Monismith SG, Steinbuck JV, Genin A. 2006 The effects of waves and morphology on mass transfer within branched reef corals. *Limnol. Oceanogr.* **51**, 1134–1141. (doi:10.4319/lo.2006.51.2.1134)
- Falter JL, Lowe RJ, Zhang Z. 2016 Toward a universal mass-momentum transfer relationship for predicting nutrient uptake and metabolite exchange in benthic reef communities. *Geophys.*

- Res. Lett.* **43**, 9764–9772. (doi:10.1002/2016GL070329)
23. Sarpkaya T. 1976 In-line and transverse forces, on cylinders in oscillatory flow at high Reynolds numbers. In *Eighth Annual Offshore Technology Conf., Houston, TX, 3–6 May*. Paper no. 0 TC 2533. Dove Valley, CO: American Institute of Mining, Metallurgical, and Petroleum Engineers, Inc. (doi:10.4043/2533-MS)
  24. Tatsuno M, Bearman PW. 1990 A visual study of the flow around an oscillating circular cylinder at low Keulegan–Carpenter numbers and low Stokes numbers. *J. Fluid Mech.* **211**, 157–182. (doi:10.1017/S0022112090001537)
  25. Sarpkaya T. 1986 Force on a circular cylinder in viscous oscillatory flow at low Keulegan–Carpenter numbers. *J. Fluid Mech.* **165**, 61–71. (doi:10.1017/S0022112086002999)
  26. Perry AE, Schofield WH, Joubert PN. 1969 Rough wall turbulent boundary layers. *J. Fluid Mech.* **37**, 383–413. (doi:10.1017/S0022112069000619)
  27. Leonardi S, Orlandi P, Antonia RA. 2007 Properties of d- and k-type roughness in a turbulent channel flow. *Phys. Fluids* **19**, 125101. (doi:10.1063/1.2821908)
  28. Li A, Reidenbach MA. 2014 Forecasting decadal changes in sea surface temperatures and coral bleaching within a Caribbean coral reef. *Coral Reefs* **33**, 847–861. (doi:10.1007/s00338-014-1162-1)
  29. Gross TF, Nowell AR. 1983 Mean flow and turbulence scaling in a tidal boundary layer. *Cont. Shelf Res.* **2**, 109–126. (doi:10.1016/0278-4343(83)90011-0)
  30. Bendat JS, Piersol AG. 2010 *Random data: analysis and measurement procedures*, 4th edn. Hoboken, NJ: John Wiley & Sons.
  31. Falter JL, Atkinson MJ, Lowe RJ, Monismith SG, Koseff JR. 2007 Effects of nonlocal turbulence on the mass transfer of dissolved species to reef corals. *Limnol. Oceanogr.* **52**, 274–285. (doi:10.4319/lo.2007.52.1.0274)
  32. Voulgaris G, Trowbridge JH. 1998 Evaluation of the acoustic Doppler velocimeter (ADV) for turbulence measurements. *J. Atmos. Ocean Technol.* **15**, 272–289. (doi:10.1175/1520-0426(1998)015<0272:EOTADV>2.0.CO;2)
  33. Bricker JD, Monismith SG. 2007 Spectral wave–turbulence decomposition. *J. Atmos. Ocean Technol.* **24**, 1479–1487. (doi:10.1175/JTECH2066.1)
  34. Stocking JB, Rippe JP, Reidenbach MA. 2016 Structure and dynamics of turbulent boundary layer flow over healthy and algae-covered corals. *Coral Reefs* **35**, 1047–1059. (doi:10.1007/s00338-016-1446-8)
  35. Wiberg P, Smith JD. 1983 A comparison of field data and theoretical models for wave current interactions at the bed on the continental shelf. *Cont. Shelf Res.* **2**, 147–162. (doi:10.1016/0278-4343(83)90013-4)
  36. Soulsby RL, Dyer KR. 1981 The form of the near-bed velocity profile in a tidally accelerating flow. *J. Geophys. Res.* **81**, 8067–8073. (doi:10.1029/JC086iC09p08067)
  37. Jonsson IG. 1966 Wave boundary layers and friction factors. In *10th Coast. Eng. Conf. September, Tokyo, Japan*. Reston, VA: American Society of Civil Engineers. (doi:10.1061/9780872620087.010)
  38. Hearn C, Atkinson M, Falter J. 2001 A physical derivation of nutrient-uptake rates in coral reefs: effects of roughness and waves. *Coral Reefs* **20**, 347–356. (doi:10.1007/s00338-001-0185-6)
  39. Laforsch C, Christoph E, Glaser C, Naumann M, Wild C, Niggli W. 2008 A precise and non-destructive method to calculate the surface area in living scleractinian corals using X-ray computed tomography and 3D modeling. *Coral Reefs* **27**, 811–820. (doi:10.1007/s00338-008-0405-4)
  40. Nicoud F, Ducros F. 1999 Subgrid-scale stress modelling based on the square of the velocity gradient tensor. *Flow Turbul. Combust.* **62**, 183–200. (doi:10.1023/A:1009995426001)
  41. Kader B. 1981 Temperature and concentration profiles in fully turbulent boundary layers. *Int. J. Heat Mass Transf.* **24**, 1541–1544. (doi:10.1016/0017-9310(81)90220-9)
  42. Sakakibara J, Hishida K, Maeda M. 1997 Vortex structure and heat transfer in the stagnation region of an impinging plane jet (simultaneous measurements of velocity and temperature fields by digital particle image velocimetry and laser-induced fluorescence). *Int. J. Heat Mass Transf.* **40**, 3163–3176. (doi:10.1016/S0017-9310(96)00367-5)
  43. Hunt JCR, Wray A, Moin P. 1988 Eddies, stream, and convergence zones in turbulent flows. *Cent. Turbul. Res. Rep.* **CTR-588**, 193–208.
  44. Edmunds PJ, Burgess SC. 2018 Colony size and turbulent flow speed modulate the calcification response of the coral *Pocillopora verrucosa* to temperature. *Mar. Biol.* **165**, 13. (doi:10.1007/s00227-017-3257-z)
  45. Kaandorp JA, Sloot PMA, Merks RMH, Bak RPM, Vermeij MJA, Maier C. 2005 Morphogenesis of the branching reef coral *Madracis mirabilis*. *Proc. R. Soc. B* **272**, 127. (doi:10.1098/rspb.2004.2934)
  46. Leonardi S, Orlandi P, Smalley RJ, Djenidi L, Antonia RA. 2003 Direct numerical simulations of turbulent channel flow with transverse square bars on one wall. *J. Fluid Mech.* **491**, 229–238. (doi:10.1017/S0022112003005500)
  47. Ryu DN, Choi DH, Patel VC. 2007 Analysis of turbulent flow in channels roughened by two-dimensional ribs and three-dimensional blocks. Part II: Heat transfer. *Int. J. Heat Fluid Flow* **28**, 1112–1124. (doi:10.1016/j.ijheatfluidflow.2006.11.007)
  48. Incropera FP, DeWitt DP. 1996 *Fundamentals of heat and mass transfer*, 4th edn. New York, NY: John Wiley and Sons.
  49. Picioreanu C, van Loosdrecht MCM, Heijnen JJ. 1997 Modelling the effect of oxygen concentration on nitrite accumulation in a biofilm airlift suspension reactor. *Water Sci. Technol.* **36**, 147. (doi:10.2166/wst.1997.0034)
  50. van Rijn LC. 2007 Unified view of sediment transport by currents and waves. II: Suspended transport. *J. Hydraul. Eng.* **133**, 668–689. (doi:10.1061/(ASCE)0733-9429(2007)133:6(668))
  51. Orlandi P, Leonardi S, Antonia RA. 2006 Turbulent channel flow with either transverse or longitudinal roughness elements on one wall. *J. Fluid Mech.* **561**, 279–305. (doi:10.1017/S0022112006000723)
  52. Shapiro OH, Fernandez VI, Garren M, Guasto JS, Debaillon-Vesque FP, Kramarsky-Winter E, Vardi A, Stocker R. 2014 Vortical ciliary flows actively enhance mass transport in reef corals. *Proc. Natl Acad. Sci. USA* **111**, 13 391–13 396. (doi:10.1073/pnas.1323094111)
  53. Enríquez S, Méndez ER, Iglesias-Prieto RI. 2005 Multiple scattering on coral skeletons enhances light absorption by symbiotic algae. *Limnol. Oceanogr.* **50**, 1025–1032. (doi:10.4319/lo.2005.50.4.1025)
  54. Jimenez IM, Kühl M, Larkum AW, Ralph PJ. 2008 Heat budget and thermal microenvironment of shallow-water corals: do massive corals get warmer than branching corals? *Limnol. Oceanogr.* **53**, 1548–1561. (doi:10.4319/lo.2008.53.4.1548)
  55. Vollmer SV, Palumbi SR. 2002 Hybridization and the evolution of reef coral diversity. *Science* **296**, 2023. (doi:10.1126/science.1069524)
  56. Sebens KP. 1984 Water flow and coral colony size: interhabitat comparisons of the octocoral *Alcyonium siderium*. *Proc. Natl. Acad. Sci. USA* **81**, 5473. (doi:10.1073/pnas.81.17.5473)
  57. Hughes TP *et al.* 2018 Global warming transforms coral reef assemblages. *Nature* **556**, 492. (doi:10.1038/s41586-018-0041-2)
  58. Loya Y, Sakai K, Yamazato K, Nakano Y, Sambali H, van Woesik R. 2001 Coral bleaching: the winners and the losers. *Ecol. Lett.* **4**, 122–131. (doi:10.1046/j.1461-0248.2001.00203.x)